Editors' Suggestion | Featured in Physics

Observation of the Magneto-Thomson Effect

Ken-ichi Uchida,[1,2,3,*] Masayuki Murata,[4] Asuka Miura,[1] and Ryo Iguchi[1]

[1]National Institute for Materials Science, Tsukuba 305-0047, Japan
[2]Institute for Materials Research, Tohoku University, Sendai 980-8577, Japan
[3]Center for Spintronics Research Network, Tohoku University, Sendai 980-8577, Japan
[4]National Institute of Advanced Industrial Science and Technology, Tsukuba, 305-8568, Japan

(Received 20 June 2020; accepted 29 July 2020; published 2 September 2020)

We report the observation of the higher-order thermoelectric conversion based on a magneto-Thomson effect. By means of thermoelectric imaging techniques, we directly observed the temperature change induced by the Thomson effect in a polycrystalline $Bi_{88}Sb_{12}$ alloy under a magnetic field and found that the magnetically enhanced Thomson coefficient can be comparable to or even larger than the Seebeck coefficient. Our experiments reveal the significant contribution of the higher-order magnetothermoelectric conversion, opening the door to "nonlinear spin caloritronics."

DOI: 10.1103/PhysRevLett.125.106601

The thermoelectric Thomson effect was predicted in the middle of the 19th century by William Thomson, known as Lord Kelvin [1,2]. When a charge current with the density $\mathbf{j}_c$ and a temperature gradient ∇T are applied to a conductor, the Thomson effect induces heat release or absorption proportional to $\mathbf{j}_c$ and ∇T [Fig. 1(a)]; the heat production rate per unit volume due to the Thomson effect is described as

$$\dot{q} = -\tau \mathbf{j}_c \cdot \nabla T, \tag{1}$$

where τ is the Thomson coefficient. The Thomson effect originates from the simultaneous operation of the Seebeck and Peltier effects, and appears when the temperature T dependence of the Seebeck coefficient S in a conductor is finite. If the charge current flows through the spatial gradient of S, the self-induced Peltier effect modulates the temperature in response to the charge current. Thus, the Thomson coefficient is related to S and the Peltier coefficient Π as

$$\tau = \frac{d\Pi}{dT} - S = T\frac{dS}{dT}. \tag{2}$$

This is the first Thomson (or Kelvin) relation, which is derived from the energy conservation and the second Thomson relation, i.e., the Onsager reciprocal relation between the Seebeck and Peltier effects: $\Pi = ST$ [3–6].

The Seebeck and Peltier coefficients are known to be dependent on a magnetic field or a magnetization direction. Such magnetothermoelectric effects are one of the central topics in the field of spin caloritronics [7,8]. However, the magnetothermoelectric effects have been investigated only in a linear response regime, and their nonlinear effects remain to be observed. In nonlinear spin caloritronics, the temperature derivative of magnetothermoelectric and/or thermospin conversion coefficients plays a key role. In fact, Eq. (2) suggests that, if a conductor exhibits the magneto-Seebeck and Peltier effects [9] with finite T dependence, τ may also depend on a magnetic field or magnetization (note that $\Pi = ST$ holds under a magnetic field if the asymmetric field dependence of the Seebeck coefficient, known as the Umkehr effect, is absent [3]). This is a nonlinear magnetothermoelectric conversion phenomenon that should be called a magneto-Thomson effect (MTE).

In this study, we report the observation of the MTE in a nonmagnetic conductor under a magnetic field and reveal its significant contribution. If the MTE appears, the magnitude of the Thomson-effect-induced temperature change is modulated by a magnetic field [Fig. 1(b)]. To demonstrate this effect, we use a polycrystalline $Bi_{88}Sb_{12}$ alloy since it shows the large temperature and magnetic field dependences of the Seebeck coefficient [10–16], which fills the requirements for the appearance of the MTE.

To achieve the direct observation of the MTE, it is important to establish a versatile measurement method for the Thomson effect. We realized highly sensitive pure detection of the temperature change induced by the Thomson effect by means of the thermoelectric imaging technique based on the lock-in thermography (LIT) [17–20]. In the LIT measurements, we measure thermal images of a sample surface while applying a square-wave-modulated ac charge current with the amplitude J_c, frequency f, and zero dc offset to the sample and extract temperature change oscillating with the same frequency as the current through Fourier analysis. Here, the obtained thermal images are transformed into the lock-in amplitude A and phase ϕ images. This analysis allows us to separate the contribution of thermoelectric effects ($\propto J_c$) from that of

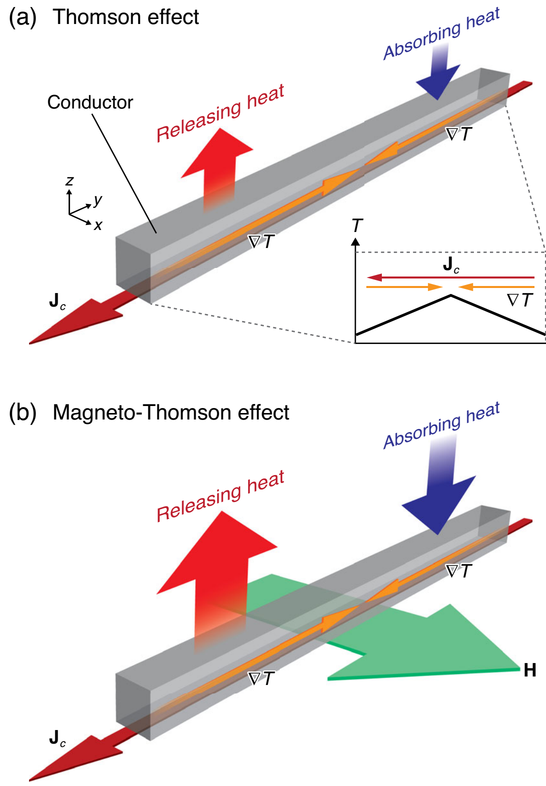

FIG. 1. Thomson and magneto-Thomson effects. (a) Schematic of the conventional Thomson effect. When a charge current $\mathbf{J}_c$ and a temperature gradient ∇T are applied to a conductor, the Thomson effect induces heat absorption or release depending on the scalar product of $\mathbf{J}_c$ and ∇T. (b) Schematic of the magneto-Thomson effect. The heat production rate due to the Thomson effect can be modulated by applying a magnetic field $\mathbf{H}$ to a conductor.

Joule heating ($\propto J_c^2$), because the Joule heating generated by such a rectangular ac current is constant in time [19,20].

Figure 2(a) shows a schematic illustration of the experimental setup for the measurements of the Thomson effect. We applied the ac charge current and static temperature gradients to a bar-shaped $Bi_{88}Sb_{12}$ slab along the y direction, where both the ends of the slab are thermally connected to heat baths (see Secs. S1 and S2 in the Supplemental Material [21–26]). The temperature gradients were generated by attaching a heater to the center of the $Bi_{88}Sb_{12}$ slab. In this configuration, the direction of the temperature gradient in the region $R1$ is opposite to that in the region $R2$, while the direction of the charge current is the same over the slab [Fig. 2(a)]. Therefore, the sign of the temperature change due to the Thomson effect is expected to be reversed between $R1$ and $R2$ [see Fig. 2(a) and Eq. (1)]. During the LIT measurements, an external magnetic field $\mathbf{H}$ with the magnitude $|\mu_0 H| \leq 0.9$ T was applied to the slab along the x direction, where μ_0 is the vacuum permeability. Although thermoelectric signals in LIT images may include the contributions of the Peltier effect generated at the ends of the $Bi_{88}Sb_{12}$ slab connecting to electrodes and the Ettingshausen effect [27–29] in the $Bi_{88}Sb_{12}$ slab under a finite magnetic field, such parasitic signals can be eliminated by subtracting LIT images measured without the temperature gradients from those with the gradients, as discussed below. The LIT measurements were carried out at room temperature and atmospheric pressure.

We start with demonstrating the validity of our LIT-based method by performing the measurements of the Thomson effect in the absence of a magnetic field. Figure 2(e) shows the steady-state temperature profiles along the y direction on the top surface of the $Bi_{88}Sb_{12}$ slab, measured with supplying finite power to the heater. The temperature distribution is as designed; the temperature gradient increases with increasing the heating power P and the direction of the gradient around $R1$ is opposite to that around $R2$. We confirmed that the temperature distribution is little affected by the Joule heating due to the charge current in the $Bi_{88}Sb_{12}$ slab. In Figs. 2(b) and 2(c), we show the A and ϕ images for the $Bi_{88}Sb_{12}$ slab at $J_c = 100.0$ mA and $f = 1.0$ Hz. The clear charge-current-induced temperature modulation was found to appear when $P = 30$ mW [Fig. 2(b)]. We also observed small but finite Peltier signals when $P = 0$ mW [Fig. 2(c)]. By subtracting the Peltier background from the signals in Fig. 2(b), we obtained the A_{TE} and ϕ_{TE} images in Fig. 2(d); hereafter, we focus on the subtracted images. As shown in the A_{TE} profiles along the y direction in Fig. 2(f), the magnitude of the current-induced temperature modulation exhibits the maximum values around $R1$ and $R2$. We checked that the magnitude of the temperature modulation increases in proportion to both the charge current and temperature gradients applied to the $Bi_{88}Sb_{12}$ slab [Figs. 2(h) and 2(i)], where the temperature gradients along the y direction were estimated by fitting the steady-state temperature profiles in $R1$ and $R2$ with linear functions [Fig. 2(e)]. Importantly, the sign of the current-induced temperature modulation at $R1$ is opposite to that at $R2$ because the ϕ_{TE} difference between $R1$ and $R2$ is $\sim 180°$ [Fig. 2(g)]. These behaviors are consistent with the features of the Thomson effect. We note that the spatial distribution of the temperature modulation in Figs. 2(d), 2(f), and 2(g) appears as a consequence of the facts that the sign of the Thomson signal is reversed across the center of the $Bi_{88}Sb_{12}$ slab and that both the ends of the slab are thermally connected to the heat baths.

Now, we are in a position to investigate the MTE by means of the LIT-based method. In Figs. 3(a) and 3(b), we compare the A_{TE} and ϕ_{TE} images at $|\mu_0 H| = 0.0$ T with those at $|\mu_0 H| = 0.9$ T. Here, we focus on the temperature modulation showing H-even dependence because the asymmetric field dependence of the Seebeck coefficient due to the Umkehr effect is negligibly small in polycrystalline Bi-Sb alloys around room temperature [16]; the extraction of temperature modulation signals with H-even

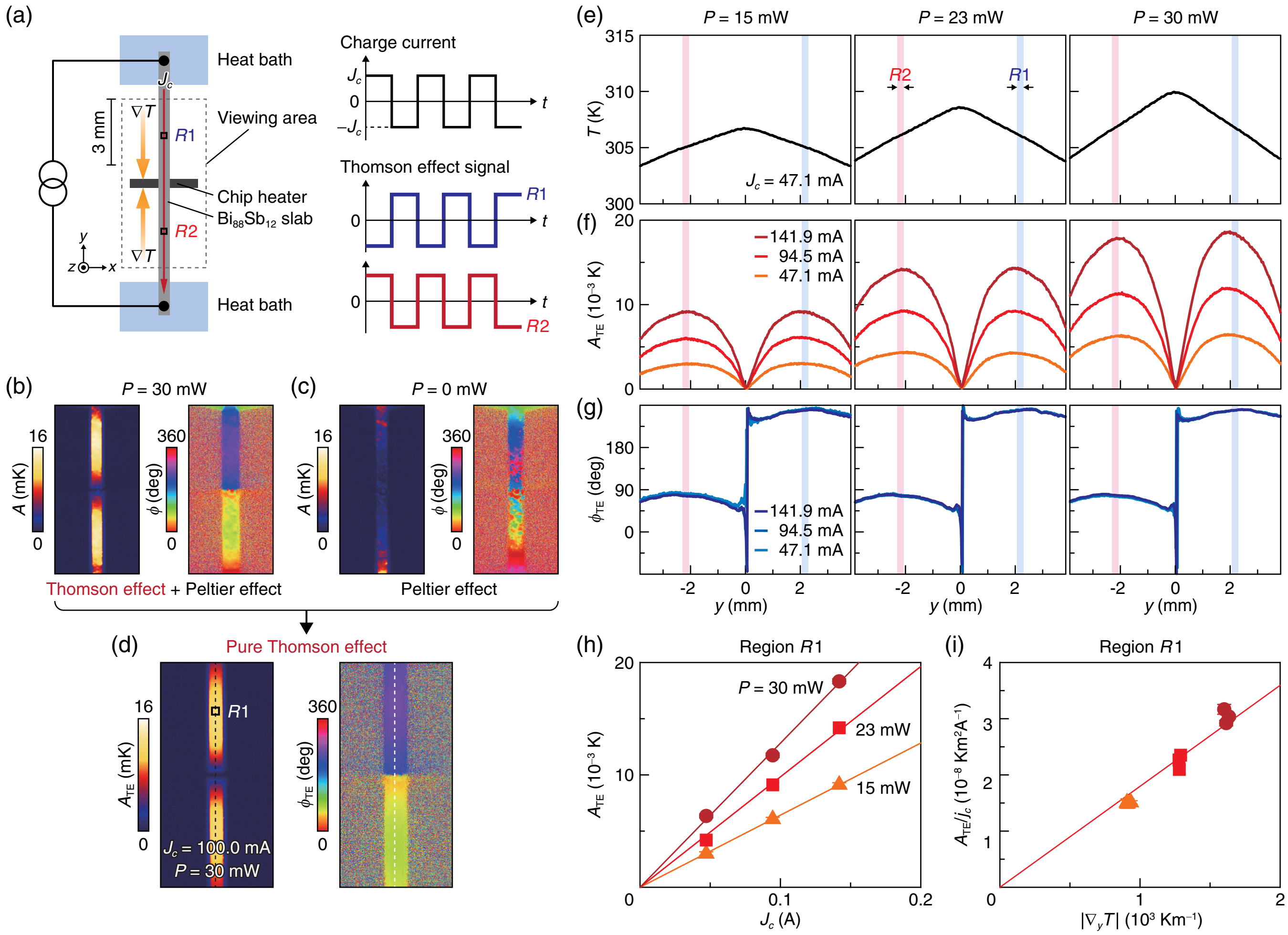

FIG. 2. Thermal imaging of Thomson effect at zero magnetic field. (a) Experimental configuration for the measurements of the Thomson effect in the $Bi_{88}Sb_{12}$ slab using the lock-in thermography method. During the measurement, a square-wave-modulated ac charge current with the amplitude J_c, frequency f, and zero dc offset was applied to the slab. The data shown in this figure were measured in the absence of an external magnetic field. (b),(c) Lock-in amplitude A and phase ϕ images for the $Bi_{88}Sb_{12}$ slab at $J_c = 100.0$ mA and $f = 1.0$ Hz, measured when the heating power P of the heater is 30 mW (b) or 0 mW (c). (d) A_{TE} and ϕ_{TE} images for the $Bi_{88}Sb_{12}$ slab, obtained by subtracting the images in (c) from those in (b). (e)–(g) Steady-state temperature T (e), A_{TE} (f), and ϕ_{TE} (g) profiles along the y direction for various values of J_c and P. The profiles were obtained by averaging 16 y-directional raw profiles along the x direction; the center of the averaged area is marked with dotted lines in (d). (h) J_c dependence of A_{TE} on the region $R1$ for various values of P. (i) $|\nabla_y T|$ dependence of A_{TE}/j_c on $R1$. j_c and $|\nabla_y T|$ denote the square-wave amplitude of the charge current density and the temperature gradient along the y direction, respectively. The data points in (h) and (i) are obtained by averaging the A_{TE} values on the area defined by the square with the size of 16×16 pixels (0.24×0.24 mm^2) in (d). The error bars represent the standard deviation of the data in the corresponding squares, which are smaller than the size of the data points.

dependence is necessary for separating the Thomson signal from the contribution of the Ettingshausen effect with H-odd dependence (see Fig. S1 in the Supplemental Material [26] for the details of background subtraction procedures in the presence of a magnetic field). The Thomson signal in the $Bi_{88}Sb_{12}$ slab was observed to be enhanced by applying the magnetic field. Figure 3(c) shows the η_{TE} values as a function of $|\mu_0 H|$ at $f = 1.0$ Hz, where $\eta_{TE} = |A_{TE}/(j_c \nabla_y T)|$ with j_c and $\nabla_y T$, respectively, being the square-wave amplitude of the charge current density and the temperature gradient along the y direction is proportional to τ [see Eq. (1) and Sec. S3 in the Supplemental Material [26,30], where the relation between η_{TE} and τ is analytically derived]. We found that the magnitude of the Thomson signal monotonically increases with increasing $|\mu_0 H|$ and the $|\mu_0 H|$ dependence of η_{TE} is independent of f, as shown in Fig. S2 in Supplemental Material [26]. Surprisingly, the enhancement ratio of the Thomson signal for the $Bi_{88}Sb_{12}$ slab reaches $[\eta_{TE}(0.9\ \mathrm{T}) - \eta_{TE}(0.0\ \mathrm{T})]/\eta_{TE}(0.0\ \mathrm{T}) = 90.3 \pm 8.3\%$ at room temperature. This is much greater than the field dependence of the linear-response transport coefficients: $[\sigma(0.9\ \mathrm{T}) - \sigma(0.0\ \mathrm{T})]/\sigma(0.0\ \mathrm{T}) = -19.4\%$ for the electrical conductivity σ [Fig. S3(a) in Supplemental

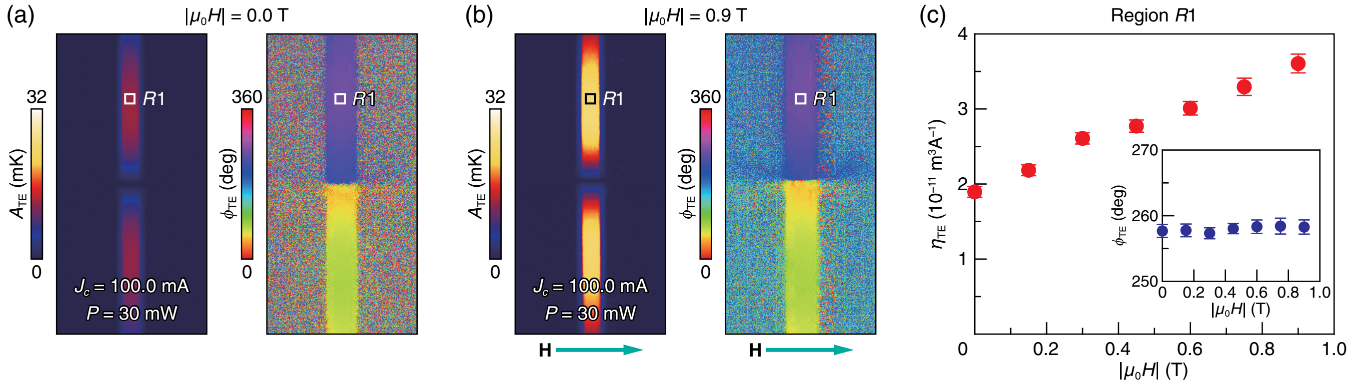

FIG. 3. Observation of magneto-Thomson effect. (a),(b) A_{TE} and ϕ_{TE} images for the $Bi_{88}Sb_{12}$ slab at $J_c = 100.0$ mA, $f = 1.0$ Hz, and $P = 30$ mW, measured when the magnetic field of $|\mu_0 H| = 0.0$ T (a) or 0.9 T (b) was applied along the x direction. (c) $|\mu_0 H|$ dependence of the Thomson signal $\eta_{TE}(= |A_{TE}/(j_c \nabla_y T)|)$ on $R1$ of the $Bi_{88}Sb_{12}$ slab. The inset to (c) shows the $|\mu_0 H|$ dependence of ϕ_{TE} on $R1$. The data points in (c) are obtained by averaging the A_{TE} and ϕ_{TE} values on the areas defined by the squares with the size of 16×16 pixels in (a) and (b). The error bars represent the standard deviation of the data in the corresponding squares.

Material [26]], $[\kappa(0.9\ \mathrm{T}) - \kappa(0.0\ \mathrm{T})]/\kappa(0.0\ \mathrm{T}) = -8.3\%$ for the thermal conductivity κ [Fig. S3(b)], and $[S(0.9\ \mathrm{T}) - S(0.0\ \mathrm{T})]/S(0.0\ \mathrm{T}) = 20.5\%$ for the Seebeck coefficient [Fig. 4(a)] of the $Bi_{88}Sb_{12}$ slab at $T = 300$ K. We also note that, in isotropic polycrystalline alloys, the MTE properties are not changed when the **H** direction is rotated in the z-x plane, where **H** is perpendicular to the charge current. In contrast, the magnetic field dependence of the Thomson signal is expected to be reduced when **H** is applied along the charge current (y direction), since the MTE in a nonmagnetic conductor originates from the Lorentz force acting on charge carriers.

To further verify the giant MTE, we systematically measured the H and T dependences of S for the same $Bi_{88}Sb_{12}$ slab, where $|\mu_0 H| \leq 1.0$ T and $270\ \mathrm{K} < T < 350$ K. As shown in Figs. 4(a) and 4(b), S is negative in the $\mu_0 H$ and T ranges and $|S|$ increases (decreases) with increasing H (increasing T). The H-even dependence of S is consistent with the expected behavior of the magneto-Seebeck effect, where the asymmetric component is negligibly small. The systematic data on the magneto-Seebeck effect allows us to estimate the $|\mu_0 H|$ dependence of τ based on Eq. (2). We found that τ monotonically increases with increasing $|\mu_0 H|$, which is similar to the $|\mu_0 H|$ dependence of η_{TE} [compare Fig. 4(c) with Fig. 3(c)]. This good consistency between the directly observed MTE and the magneto-Seebeck effect confirms the validity of the first Thomson relation under a magnetic field. The observed Thomson coefficient of our polycrystalline $Bi_{88}Sb_{12}$ reaches $\tau = 98.3 \times 10^{-6}\ \mathrm{V\,K^{-1}}$ at $|\mu_0 H| = 0.9$ T and $T = 300$ K, which is comparable to its Seebeck coefficient. Our finding indicates that the Thomson coefficient enhanced by the MTE can even be larger than the Seebeck coefficient under stronger magnetic fields, highlighting the significant contribution of the higher-order magnetothermoelectric conversion.

As shown above, we have investigated the MTE in a nonmagnetic conductor under a magnetic field. It is also interesting to measure the Thomson effect in magnetic materials. The observation of the anisotropic magneto-

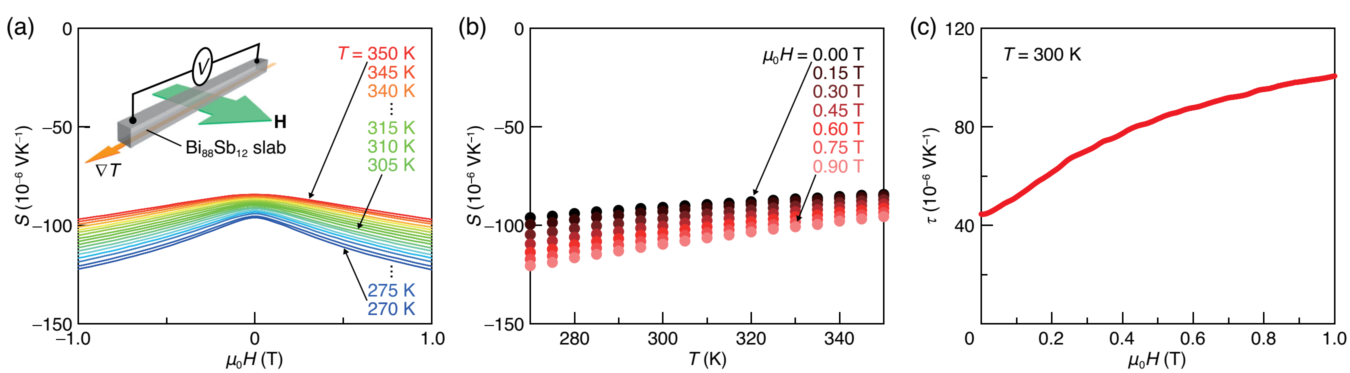

FIG. 4. Magnetic field and temperature dependences of Seebeck coefficient. (a) $\mu_0 H$ dependence of the Seebeck coefficient S of the $Bi_{88}Sb_{12}$ slab for various values of T. (b) T dependence of S for various values of $\mu_0 H$. (c) $\mu_0 H$ dependence of the Thomson coefficient τ at $T = 300$ K, calculated from the data in (a) and (b) based on Eq. (2).

Seebeck and Peltier effects in ferromagnetic metals [20,31–36], in which the Seebeck and Peltier coefficients depend on the direction of spontaneous magnetization, suggests the possible existence of an anisotropic MTE; however, this phenomenon is yet to be observed. To investigate the anisotropic MTE, we performed the same LIT measurements using ferromagnetic $Ni_{95}Pt_5$ and Ni slabs, which exhibit the substantially large anisotropic magneto-Seebeck and Peltier effects at room temperature [20,36]. As shown in Figs. S4(a)–S4(c) in Supplemental Material [26], we observed clear temperature modulation signals due to the Thomson effect in the $Ni_{95}Pt_5$ and Ni slabs and found that the sign of the temperature modulation for the ferromagnets is opposite to that for the $Bi_{88}Sb_{12}$ slab [compare Figs. S4(b) and S4(c) in Ref. [26] with Figs. 3(a) and 3(b)]. This behavior can be explained by the fact that the $T(dS/dT)$ values for $Ni_{95}Pt_5$ and Ni are opposite in sign to those for $Bi_{88}Sb_{12}$ (Figs. 4 and S5 in Supplemental Material [26]). However, we found that the Thomson signals for $Ni_{95}Pt_5$ and Ni are an order of magnitude smaller than those for $Bi_{88}Sb_{12}$ and almost independent of the magnetization [Figs. S4(d) and S4(e) [26]], indicating that no anisotropic MTE signals appear in these ferromagnets within the margin of experimental errors. To realize the observation of the anisotropic MTE, further physics research for understanding its microscopic mechanism and materials science research for exploring ferromagnets with large anisotropy of the Thomson coefficient are necessary.

In summary, we have realized the direct observation of the MTE in the polycrystalline $Bi_{88}Sb_{12}$ slab under a magnetic field by means of the thermoelectric imaging technique based on the LIT. The temperature change induced by the Thomson effect in the $Bi_{88}Sb_{12}$ slab was found to be strongly enhanced with increasing the magnetic field; the enhancement ratio at room temperature reaches $90.3 \pm 8.3\%$ under a relatively low magnetic field of 0.9 T. The giant MTE clarifies the importance of the nonlinear magnetothermoelectric conversion and provides an unconventional concept for thermal energy engineering. The establishment of the direct measurement method for the MTE is also important for further development of spin caloritronics. Our technique is directly applicable to the measurements of the anisotropic MTE in magnetic materials, as discussed above. In addition to the anisotropic MTE, various higher-order thermoelectric and thermospin conversion phenomena, e.g., Thomson effects for spin currents and spin waves [37,38], should exist in magnetic and spintronic materials if the temperature derivative of magnetothermoelectric and/or thermospin conversion coefficients is finite. This work is the first step for investigating physics and applications of such unexplored phenomena.

The authors thank T. Seki and T. Kikkawa for valuable discussions and M. Isomura and J. Uzuhashi for technical supports. This work was supported by Grant-in-Aid for Scientific Research (B) (JP19H02585) from JSPS KAKENHI, Japan, CREST "Creation of Innovative Core Technologies for Nano-enabled Thermal Management" (JPMJCR17I1) from JST, Japan, and "Mitou challenge 2050" (P14004) from NEDO, Japan. A. M. is supported by JSPS through Research Fellowship for Young Scientists (JP18J02115).

*Corresponding author.
UCHIDA.Kenichi@nims.go.jp

[1] W. Thomson, Proc. R. Soc. Edinburgh **3**, 91 (1851).
[2] W. Thomson, Trans. R. Soc. Edinburgh **21**, 123 (1854).
[3] R. Wolfe and G. E. Smith, Phys. Rev. **129**, 1086 (1963).
[4] R. B. Roberts, Philos. Mag. **36**, 91 (1977).
[5] Y. Apertet and C. Goupil, Int. J. Therm. Sci. **104**, 225 (2016).
[6] A. M. Steane, *Thermodynamics* (Oxford University Press, Oxford, 2016).
[7] G. E. W. Bauer, E. Saitoh, and B. J. van Wees, Nat. Mater. **11**, 391 (2012).
[8] S. R. Boona, R. C. Myers, and J. P. Heremans, Energy Environ. Sci. **7**, 885 (2014).
[9] J. P. Jan, in *Solid State Physics*, edited by F. Seitz and D. Turnbull (Academic, New York, 1957), Vol. 5, pp. 1–96.
[10] R. Wolfe and G. E. Smith, Appl. Phys. Lett. **1**, 5 (1962).
[11] C. B. Thomas and H. J. Goldsmid, Phys. Lett. **27A**, 369 (1968).
[12] S. S. Li and T. A. Rabson, Solid State Electron. **13**, 153 (1970).
[13] W. M. Yim and A. Amith, Solid State Electron. **15**, 1141 (1972).
[14] T. Teramoto, T. Komine, M. Kuraishi, and R. Sugita, J. Appl. Phys. **103**, 043717 (2008).
[15] H. Jin, C. M. Jaworski, and J. P. Heremans, Appl. Phys. Lett. **101**, 053904 (2012).
[16] M. Murata, A. Yamamoto, Y. Hasegawa, and T. Komine, J. Electron. Mater. **45**, 1875 (2016).
[17] O. Breitenstein, W. Warta, and M. Langenkamp, *Lock-in Thermography: Basics and Use for Evaluating Electronic Devices and Materials* (Springer Science & Business Media, Berlin, 2010).
[18] O. Wid, J. Bauer, A. Müller, O. Breitenstein, S. S. P. Parkin, and G. Schmidt, Sci. Rep. **6**, 28233 (2016).
[19] S. Daimon, R. Iguchi, T. Hioki, E. Saitoh, and K. Uchida, Nat. Commun. **7**, 13754 (2016).
[20] K. Uchida, S. Daimon, R. Iguchi, and E. Saitoh, Nature (London) **558**, 95 (2018).
[21] B. Lenoir, H. Scherrer, and T. Caillat, in *Semiconductors and Semimetals*, edited by T. M. Tritt (Academic Press, San Diego, 2001), Vol. 69, chap. 4, pp. 101–137.
[22] V. M. Grabov and O. N. Uryupin, *Thermoelectrics Handbook: Macro to Nano*, edited by D. M. Rowe (CRC Press, Boca Raton, 2006).
[23] T. Kikkawa, K. Uchida, S. Daimon, Z. Qiu, Y. Shiomi, and E. Saitoh, Phys. Rev. B **92**, 064413 (2015).
[24] K. Vandaele, M. Otsuka, Y. Hasegawa, and J. P. Heremans, J. Phys. Condens. Matter **30**, 403001 (2018).

[25] S. Gao, J. Gaskins, X. Hu, K. Tomko, P. Hopkins, and S. J. Poon, Sci. Rep. **9**, 14892 (2019).

[26] See Supplemental Material at http://link.aps.org/supplemental/10.1103/PhysRevLett.125.106601 for the details of the sample preparation processes, measurement procedures, relation between the Thomson coefficient and lock-in thermography signals, and supplemental figures.

[27] A. V. Ettingshausen and W. Nernst, Ann. Phys. (N.Y.) **265**, 343 (1886).

[28] K. F. Cuff, R. B. Horst, J. L. Weaver, S. R. Hawkins, C. F. Kooi, and G. M. Enslow, Appl. Phys. Lett. **2**, 145 (1963).

[29] T. C. Harman, J. M. Honig, S. Fischler, A. E. Paladino, and M. J. Button, Appl. Phys. Lett. **4**, 77 (1964).

[30] M. Otsuka, R. Homma, and Y. Hasegawa, J. Electron. Mater. **46**, 2752 (2017).

[31] J.-E. Wegrowe, A. Q. Nguyen, M. Al-Barki, J.-F. Dayen, T. L. Wade, and H.-J. Drouhin, Phys. Rev. B **73**, 134422 (2006).

[32] A. D. Avery, M. R. Pufall, and B. L. Zink, Phys. Rev. Lett. **109**, 196602 (2012).

[33] M. Schmid, S. Srichandan, D. Meier, T. Kuschel, J.-M. Schmalhorst, M. Vogel, G. Reiss, C. Strunk, and C. H. Back, Phys. Rev. Lett. **111**, 187201 (2013).

[34] K. S. Das, F. K. Dejene, B. J. van Wees, and I. J. Vera-Marun, Phys. Rev. B **94**, 180403(R) (2016).

[35] O. Reimer, D. Meier, M. Bovender, L. Helmich, J.-O. Dreessen, J. Krieft, A. S. Shestakov, C. H. Back, J.-M. Schmalhorst, A. Hütten, G. Reiss, and T. Kuschel, Sci. Rep. **7**, 40586 (2017).

[36] A. Miura, R. Iguchi, T. Seki, K. Takanashi, and K. Uchida, Phys. Rev. Mater. **4**, 034409 (2020).

[37] A. Starkov and A. S. Starkov, IEEE Trans. Magn. **54**, 4500106 (2018).

[38] A. Starkov, O. V. Pakhomov, and A. S. Starkov, J. Magn. Magn. Mater. **496**, 165949 (2020).